RSC Advances

PAPER

View Article Online
View Journal | View Issue

Cite this: *RSC Adv.*, 2019, **9**, 19236

Metal–organic framework-derived CeO_2–ZnO catalysts for C_3H_6-SCR of NO: an *in situ* DRIFTS study

Ling Zhao, *[ab] Yu Zhang,[a] Sining Bi[a] and Qifeng Liu*[a]

Received 25th April 2019
Accepted 23rd May 2019

DOI: 10.1039/c9ra03103k

rsc.li/rsc-advances

Metal–organic framework (MOF)-based derivatives have attracted an increasing interest in various research fields. Here, we synthesized CeO_2–ZnO catalysts through the complete thermal decomposition of the Ce/MOF-5 precursor. The catalysts were characterized using XRD, FTIR, TG-DSC, SEM and H_2-TPR. It is found that the as-prepared CeO_2–ZnO is favorable for strengthening the interaction between Ce^{4+} and Zn^{2+}. A significant improvement in the catalytic performance for C_3H_6-SCR of NO was found over the Ce-doped catalysts with the highest N_2 yield of 69.1% achieved over 5% CeO_2–ZnO. *In situ* DRIFTS and NO-TPD experiments demonstrated the formation of monodentate nitrates, bidentate nitrates, chelating nitrite, nitro compounds, nitrosyl and $C_xH_yO_z$ species (enolic species and acetate) on the surface, followed by the formation of hydrocarbonate or carbonate as intermediates to directly generate N_2, CO_2 and H_2O.

1. Introduction

It is particularly notorious that the sheer quantity of gasoline and diesel powered vehicles grows with each passing day. The nitrogen oxides (NO_x) from automobile exhaust gases have aroused significant concern among the public and government officials because these gases can cause a great threat to the environment and public health, including the greenhouse effect, acidification, photochemical smog, and ozone depletion.[1,2] Owing to the ground-breaking work of Iwamoto *et al.*, hydrocarbon-selective catalytic reduction (HC-SCR) has become a promising technology for clearing NO_x away from the automobile exhausts, taking into account the cost and gas components, as well as the hydrocarbons coexisting with NO in the exhaust streams.[3,4] Different kinds of hydrocarbons have been employed to improve the performance of HC-SCR, including propene,[5] methane,[6] ethanol,[7] ethylene,[8] and propane.[9] More importantly, catalysts are the core of this catalytic technology. Thus, huge efforts are dedicated to develop catalysts by both the academic community and catalyst manufacturers.

Metal–organic frameworks (MOFs) are a kind of crystalline porous materials with a periodic network structure formed by the self-assembly of inorganic metals (metal ions or clusters) and bridged organic ligands.[10–14] On account of their low-density structures, tunable cavities, high surface area, tailorable chemistry and facile synthesis,[10,11] MOFs are good candidates for applications in gas separation and storage, as well as catalysis.[12–14] Recently, researchers gradually shifted their focus from MOFs to MOF derivatives.[15,16] During the calcination process, MOFs are completely decomposed and gradually converted to metal oxides from the outer to inner part. Small cavities and open channels within the MOF-derived metal oxides provide pathways for the reactant species to diffuse in and out, thus enabling these metal oxides to be suitable candidates for catalysts or catalyst supports. By way of illustration, Ce–MOF was used to prepare the CeO_2 catalyst for toluene combustion,[16] and Cu-based MOFs were applied as the precursors to attain carbon-based catalysts for low-temperature $DeNO_x$.[15] Therefore, the development of efficient functional MOF-derived metal oxides for further exploration of their practical applications has great significance.[17] More importantly, the composite materials usually exhibit excellent performances for environmental catalytic reactions. For example, Yang *et al.* prepared different functional composites and studied their outstanding performance of catalytic oxidative desulfurization and atrazine degradation.[18,19]

Cerium oxide is an extensively used promoter or catalyst support for the SCR reaction due to its superior oxygen storage capability and excellent redox properties.[15] The oxygen vacancies are produced during the electron transfer between Ce^{3+} and Ce^{4+}. The reduction of Ce^{4+} to Ce^{3+} and enhanced oxygen transfer could facilitate the oxidation process of NO to NO_2, leading to excellent HC-SCR performance.[20] In addition, it can not only highly disperse the metals but also strengthen the thermal stability in reaction with other metal oxides.[21]

In the present study, we synthesized ZnO and CeO_2–ZnO catalysts through the complete thermal decomposition of MOF-5 and Ce/MOF-5 precursor, and then compared their activity in HC-SCR. C_3H_6 was used as the reducing agent due to it being

[a]School of Ecology and Environment, Inner Mongolia University, China. E-mail: nmzhl@hotmail.com

[b]Center for Environmental and Human Toxicology, Department of Physiological Sciences, College of Veterinary Medicine, University of Florida, USA

the major hydrocarbon component during the process of automobile exhaust emissions. First, the crystal structure, morphology and textural properties of the samples were investigated *via* XRD, TG-DSC, SEM, FTIR and H_2-TPR. Second, the adsorption and activation abilities of NO were studied using temperature-programmed desorption (TPD). In addition, the *in situ* DRIFTS experiments were performed to illuminate the C_3H_6-SCR process as well as the possible reaction pathways.

2. Experimental

2.1. Materials

All of the reactants are of analytical grade and were used without further purification. $Zn(NO_3)_2\cdot 6H_2O$ and $Ce(NO_3)_2\cdot 6H_2O$ were purchased from Sinopharm Chemical Reagent Co., Ltd. 1,4-Benzenedicarboxylic acid (H_2BDC), *N*,*N*-dimethylformamide (DMF) and dichloromethane (CH_2Cl_2) were purchased from Macklin.

2.2. Catalyst preparation

MOF-5 was prepared by the solvothermal method according to the following procedures. First, 9.360 g $Zn(NO_3)_2\cdot 6H_2O$ and 2.540 g H_2BDC were dissolved in 190 ml *N*,*N*-dimethylformamide (DMF), and the resulting suspension was sonicated for 30 min. Second, the mixture was transferred into a 250 ml Teflon-lined stainless steel reactor. Then, the autoclave was placed into an oven at 120 °C for 24 h to obtain the white crystals. Subsequently, they were repetitively washed with *N*,*N*-dimethylformamide (DMF) and dichloromethane (CH_2Cl_2). Finally, the homogeneous material obtained was oven-dried at 120 °C for 12 h.

An impregnation technique was used to synthesize Ce/MOF-5. Namely, the predetermined amount of cerium nitrate ($Ce(NO_3)_2\cdot 6H_2O$) and MOF-5 precursor were dissolved in ethyl alcohol and the mixed solution was sonicated for 30 min. Afterward, the mixture was left to equilibrate at room temperature for 24 h. Finally, the product was dried at 100 °C for 12 h, followed by calcination at 600 °C for 2 h under air to obtain the CeO_2–ZnO catalysts, and were denoted as 1% CeO_2–ZnO, 3% CeO_2–ZnO, 5% CeO_2–ZnO, and 10% CeO_2–ZnO.

2.3. Catalysts characterization

In the present study, we adopted a series of methods to evaluate the crystal structure, morphology, thermal stability, reducibility and adsorption properties of the catalysts. XRD patterns were gained on the Empyrean (PANalytical B.V.) using Cu Kα radiation and the X-ray tube was operated under 40 kV and 40 mA. All the as-synthesized samples were scanned over the 2θ range between 5° and 80° at a scan speed of 10° min^{-1}. The surface morphology of all the samples was characterized by SEM (S-4800, Japan). Thermogravimetric and differential scanning calorimetry (TG-DSC) analysis curves were obtained using a STA409pc (NETZSCH German) synchronous thermal analyzer. The samples were heated from 30 °C to 700 °C at a rate of 5 °C min^{-1} under a flow of nitrogen at 40 ml min^{-1}. Hydrogen temperature-programmed reduction (H_2-TPR) and NO temperature-programmed desorption (NO-TPD) were performed on a Chembet PULSAR TPR/TPD chemisorption analyzer loaded with 50 mg samples. Prior to the reduction, the sample was pretreated under pure He atmosphere at 350 °C for 30 min for the sake of removing the absorbent (*e.g.*, H_2O). In the case of H_2-TPR, the sample began from room temperature to 800 °C under an H_2 stream at a rate of 10 °C min^{-1}. For NO-TPD, the sample was treated in a flow of NO at 100 °C for 60 min, followed by heating from 100 °C to 300 °C for desorption at a rate of 10 °C min^{-1}. Fourier transform infrared spectroscopy (FT-IR) was performed on a VERTEX German infrared spectrometer with the KBr pellet technique at room temperature. Spectra were collected in the range of 4000–400 cm^{-1} at a resolution of 4 cm^{-1}.

2.4. Catalytic performance test

The C_3H_6-SCR catalytic tests were performed in a fixed-bed quartz tube reactor. Prior to an experiment, a catalyst (200 mg) was pretreated at 300 °C for 1 h in an Ar stream, and the activity measurement was carried out from 150 °C to 350 °C at a heating rate of 10 °C min^{-1}. The reaction conditions were as follows: 1000 ppm NO, 1000 ppm C_3H_6, 5 vol% O_2 and Ar as balance; the total gas flow rate was 100 ml min^{-1} and the GHSV was 30 000 h^{-1}. The concentrations of N_2 in the effluent gas were analyzed on-line using a gas chromatograph. The conversion of NO to N_2 was calculated as follows:

$$\text{NO conversion to } N_2 = 2[N_2]_{out}/[NO]_{in} \times 100\% \quad (1)$$

2.5. *In situ* DRIFTS measurements

NO and C_3H_6 adsorption on the catalysts were recorded using a FT-IR spectrometer (VERTEX German). Concentrations of the reactants were 1000 ppm of NO, 1000 ppm of C_3H_6, 5 vol% oxygen. The sample (20 mg) was mounted in a quartz DRIFTS cell and activated by calcination in Ar stream (30 ml min^{-1}) at 300 °C for 30 min before introducing the reaction mixtures, followed by cooling to the desired temperature, and then the spectrum was collected and used as the background. All spectra were recorded at a resolution of 4 cm^{-1} (number of scans, 32) in the range of 4000–400 cm^{-1}.

3. Results and discussion

3.1. Physical and texture characterizations

From the X-ray diffraction profiles, we can identify the transformation in the phase texture on the MOF-5, MOF-5-derived ZnO and CeO_2–ZnO samples. Fig. 1(a) exhibits the previous diffraction peaks for MOF-5; the 2θ angles of 6.85°, 9.62°, 13.69°, 15.39° correspond to the (200), (220), (400), (420) planes.[11] A sharp peak appeared at 6.85°, which proved that we successfully synthesized the MOF-5 materials with high crystallinity.[11] From the MOF-5-derived composite characterization, it can be observed that the primary structure of the framework collapsed and the characteristic diffraction peaks completely

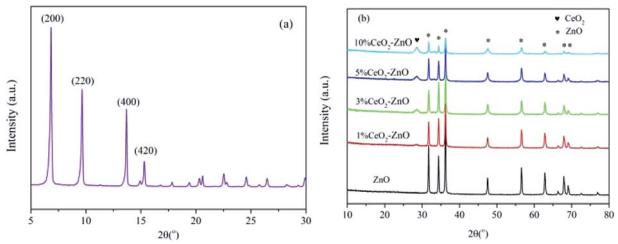

Fig. 1 XRD pattern of (a) MOF-5 and (b) ZnO and CeO_2–ZnO.

disappeared, with the main peaks of the wurtzite ZnO structure appearing at 31.7° (100), 34.4° (002), 36.3° (101), 47.4° (102), 56.6° (110), 62.8° (103), 67.9° (112) and 69.1° (201) (JCPDS No. 36-1451).[22] The sample with Ce loading also displays an additional XRD peak corresponding to the structure of CeO_2, indicating that the doped-Ce species exists in the form of CeO_2 (Fig. 1(b)).

The thermogravimetric and differential scanning calorimetry (TG-DSC) curves of the fresh MOF-5 are shown in Fig. 2. Three noticeable weight loss events were evident. The continuous weight loss of about 4% at the temperature range between 50 °C and 100 °C was caused by the evaporation of water from the surface of the sample. The second major loss in the temperature range of 150–320 °C was about 27%, which was related to the evaporation and decomposition of residual organic components (DMF).[23] The most prominent weight loss appeared at a temperature over 420 °C, and the weight loss rapidly reached almost 60%, demonstrating that the MOF-5 framework had collapsed. According to the previous study, for MOF-5, the breakdown of the carboxylic bridges between the benzene rings and Zn_4O clusters results in the decomposition of the organic ligand molecules to form CO_2 and benzene.[11] The DSC curve also shows a sharp exothermic peak between 420 °C and 485 °C with a maximum peak temperature at 480 °C due to the decomposition of the organic components. The decomposition process was completed after 550 °C. The evidence from the thermogravimetric analysis verified that the MOF-5 crystal transformed into ZnO completely above 550 °C. In view of these results, we chose 600 °C as the calcination temperature to attain the oxides.

The FTIR spectra of the as-prepared MOF-5-derived ZnO and CeO_2–ZnO catalysts are shown in Fig. 3. A significant peak at 430 cm^{-1} may be attributed to the Zn–O stretching vibrations.[23] The band at 1620 cm^{-1} is ascribed to the bond stretching of the carboxyl (O=C–OH) functional groups on the surface of the samples.[24]

3.2. Morphology

Scanning electron microscopy is a technique that enables the study of the microstructure of nanoparticles. The scanning electron micrographs of MOF-5, and the MOF-5-derived ZnO and CeO_2–ZnO catalysts are presented in Fig. 4. The MOF-5 samples clearly exhibit the cubic morphology with smooth facets and the particle size ranged from 200 nm to 500 nm (Fig. 4(a)). After thermal treatment at 600 °C, the MOF-5-derived ZnO and CeO_2–ZnO catalysts (Fig. 4(b) and (c)) mainly maintain the cubic structure, but the edge becomes smooth and the surface appears porous. In addition, compared to MOF-5, the particle sizes of the ZnO and CeO_2–ZnO catalysts show a slight decrease. During the heat-treatment of MOF-5 and Ce/MOF-5, as expected, they gradually decompose with time, resulting in the smaller and porous particles with cubic structure.

3.3. H_2-TPR measurements

H_2-TPR analysis was performed to determine the reducibility of the MOF-5-derived ZnO and CeO_2–ZnO catalysts. As shown in Fig. 5, one obvious hydrogen consumption peak centered at 600 °C exists in each sample. Compared with the ZnO catalyst, the CeO_2–ZnO catalyst presented an obvious shift towards lower temperatures with the increasing amount of Ce, suggesting that the redox properties of the catalysts were enhanced by the interaction between CeO_2 and ZnO. The enhanced redox properties could lead to a better dispersion, promoting oxygen mobility and the oxidation process of NO to NO_2.

3.4. Catalytic test

The N_2 yield as a function of temperature over the MOF-5-derived ZnO and CeO_2–ZnO catalysts is shown in Fig. 6. The MOF-5-derived ZnO achieved the maximum N_2 yield of 31.5% at 250 °C, while the activity of the Ce-doped catalysts was enhanced significantly, though the temperature corresponding to the maximum N_2 yield shifted to a higher temperature at 270 °C. Among the tested catalysts, 3% CeO_2–ZnO and 5% CeO_2–ZnO exhibited outstanding catalytic performances, with a maximum N_2 yield of 68.3% and 69.1%, respectively. The

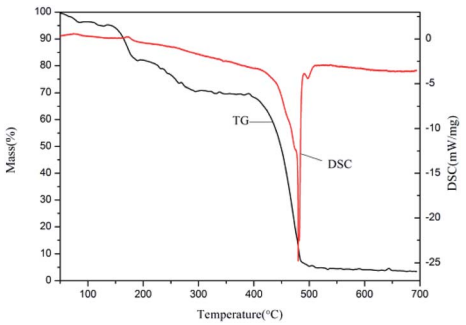

Fig. 2 TG profile for the MOF-5 precursor.

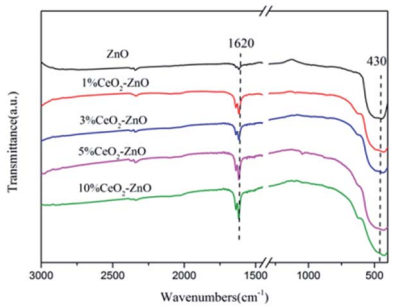

Fig. 3 FT-IR spectra of ZnO and CeO_2–ZnO catalysts.

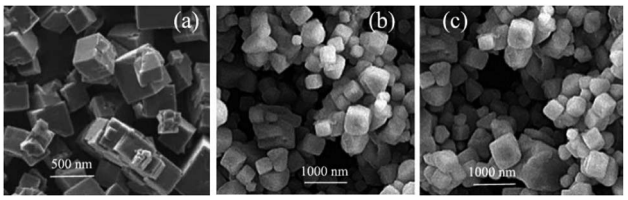

Fig. 4 SEM images of (a) MOF-5, (b) ZnO and (c) CeO_2–ZnO.

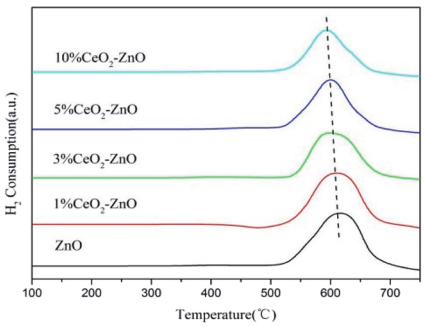

Fig. 5 H_2-TPR spectra of the ZnO and CeO_2–ZnO catalysts.

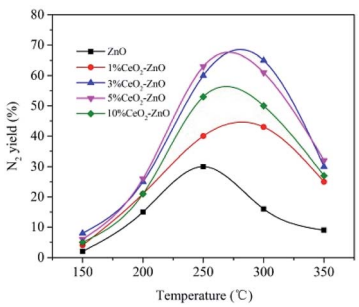

Fig. 6 N_2 yield as a function of temperature for the ZnO and CeO_2–ZnO catalysts.

unsatisfactory performance of the 10% CeO_2–ZnO catalyst (55.7%) may be attributed to the agglomeration of excess Ce.

3.5. NO-TPD measurements

To evaluate the NO adsorption ability of the as-synthesized catalyst, NO-TPD measurements were conducted to explore the interaction between NO and the samples (Fig. 7). For the MOF-5-derived ZnO catalyst, two NO desorption peaks at 176 and 219 °C could be observed. The two peaks shifted to higher temperatures after Ce was added to the catalysts, indicating that Ce can largely strengthen the bonding of NO with the catalyst surface. Moreover, the intensities of the two NO desorption peaks enhanced after the addition, which indicated that adding Ce can result in the redistribution of the adsorbed NO_x species, thus facilitating the NO oxidation. It is worth noting that the promotion effect enhanced very slowly after Ce loading, reaching over 10%. This might be caused by agglomeration of the excess Ce.

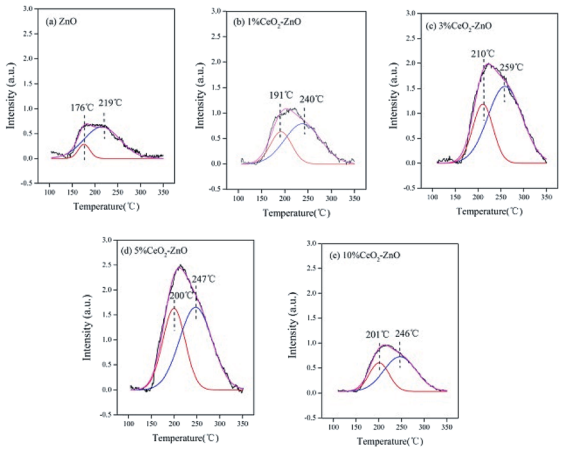

Fig. 7 NO-TPD profiles of the ZnO and CeO_2–ZnO catalysts.

3.6. DRIFTS studies

3.6.1. Adsorption of NO followed by C_3H_6/O_2 over time. In order to investigate the surface reactions and intermediates, a series of *in situ* DRIFTS experiments were performed. Fig. 8 shows the *in situ* DRIFTS spectra obtained after exposure to 1000 ppm NO and 5% O_2 in Ar, followed by 1000 ppm C_3H_6 and 5 vol% O_2 in Ar at 250 °C. In the case of the MOF-5-derived ZnO catalyst (Fig. 8(a)), NO and O_2 flushing at 250 °C produced several bands. The bands at 1122 cm^{-1} and 1582 cm^{-1} are attributed to the bidentate nitrates,[25,26] which are formed when the NO molecules bridge two adjacent oxygen atoms.[25] In addition, the nitrosyl (adsorbed NO) (1845 cm^{-1} and 1900 cm^{-1}),[27,28] hydroxyl group (3705 cm^{-1} and 3738 cm^{-1}),[27,28] and gas phase CO_2 (2355 cm^{-1})[29] also appeared. Upon switching to C_3H_6 and O_2, the surface bidentate nitrates decreased slightly with time, while the other bands remained unchanged.

In the case of the 1% CeO_2–ZnO catalyst (Fig. 8(b)), the formation of monodentate nitrate, chelating nitrite and gas-phase NO (1028 cm^{-1}, 1180 cm^{-1} and 1634 cm^{-1}, respectively) occurred on the surface after 10 min and was slightly enhanced with increasing time. Switching to the C_3H_6/O_2 mixture, several new bands were detected. The bands at

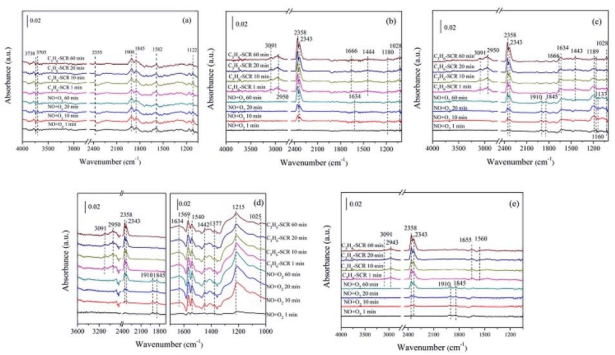

Fig. 8 *In situ* DRIFTS of (a) ZnO, (b) 1% CeO_2–ZnO, (c) 3% CeO_2–ZnO (d) 5% CeO_2–ZnO (e) 10% CeO_2–ZnO exposed to the SCR reaction at 250 °C for various times under NO + O_2 adsorption and during C_3H_6 interaction with the NO + O_2 gas mixture.

1666 cm^{-1} and 1444 cm^{-1} are assigned to the enolic species (RCH=CH–O^-) and acetic acid, respectively.[27,28] The IR bands centered at 2950 cm^{-1} and 3091 cm^{-1} are attributed to the asymmetric and symmetric CH stretch (νCH) of the CH_3 group, which were proposed by Efstathiou *et al.* to indicate the –CH_3 adsorbed species produced from the interaction of C_3H_6 with the catalyst surface.[30] In addition, a large amount of gas phase CO_2 was observed at 2343 cm^{-1} and 2358 cm^{-1}.

For the 3% CeO_2–ZnO catalyst (Fig. 8(c)), NO/O_2 flushing after 1 min produced the monodentate nitrate (at 1028 and 1137 cm^{-1}), chelating nitrite (at 1160 and 1189 cm^{-1}), nitrosyl (at 1845 cm^{-1} and 1910 cm^{-1}), and gas-phase NO (at 1634 cm^{-1}), indicating that the 3% CeO_2–ZnO catalyst exhibited better adsorption performance in comparison with the 1% CeO_2–ZnO catalyst. In addition, the peaks at 2343 and 2358 cm^{-1} belong to the gas phase CO_2 and are attributed to the C=O bonds on the carbon surface. The intensities of these peaks were markedly increased by prolonging the adsorption time. Similar to the 1% CeO_2–ZnO catalyst, the chelating nitrite and nitrosyl group clearly decreased after purging with C_3H_6/O_2, accompanied by an appearance of the enolic species (1666 cm^{-1}) and acetate (1443 cm^{-1}) over 3% CeO_2–ZnO.

In the case of the 5% CeO_2–ZnO catalyst (Fig. 8(d)), excluding the similar characteristic peaks with the 1% CeO_2–ZnO and 3% CeO_2–ZnO catalysts, several new bands such as the bidentate nitrate (1569 and 1540 cm^{-1}) and nitro compounds (1280 cm^{-1}) were observed at the same time, suggesting the enhanced adsorption ability of NO on the 5% CeO_2–ZnO catalyst. For 10% CeO_2–ZnO (Fig. 8(e)), the peaks were significantly weakened, revealing that the doping amount of cerium should be appropriate for the ceria–zinc mixed oxides.

On the basis of these facts, we can reach the following conclusion. The nitrates (monodentate nitrates, bidentate nitrates), chelating nitrite, nitro compounds and nitrosyl groups are formed on the surface of the catalysts from the interaction of NO and O_2. After introducing C_3H_6, these species decreased or diminished, accompanied by hydrocarbonate, enolic species and acetate. In addition, significant amounts of gas phase CO_2 and H_2O (the products of C_3H_6 oxidation) were also observed. All of the bands were significantly enhanced by adding ceria.

3.6.2. Adsorption of C_3H_6/O_2 followed by NO at 250 °C on the 5% CeO_2–ZnO catalyst. To determine the adsorption and activation of C_3H_6 in the presence of O_2 and to study the reactivity of the adsorbed NO_x species, a mixture of C_3H_6 and O_2, followed by NO were flowed over the catalysts at 250 °C. The DRIFTS spectra of the ZnO catalyst were not apparent here; thus, we selected the 5% CeO_2–ZnO catalyst for the DRIFTS measurements. As observed in Fig. 9, after purging with C_3H_6/O_2, the C–H bending mode of the –CH_3 group for the adsorbed hydrocarbonate could be observed by the band at 1440 cm^{-1}. The –CH stretching vibrations (2953 cm^{-1} and 3101 cm^{-1}) were assigned to the unsaturated hydrocarbon fragments. In addition, the bands for $C_xH_yO_z$ (at 1636 cm^{-1}) and C_3H_6 in the gas phase (at 1666 cm^{-1}) were recorded.

Exposure to NO resulted in the surface $C_xH_yO_z$, hydrocarbonate and C_3H_6 gas fade away, combined with an enhancement in the bidentate nitrate (at 1598 cm^{-1}) and nitrosyl (at 1845 cm^{-1} and 1910 cm^{-1}) species. More importantly, the formation of CO_2 (2358 and 2343 cm^{-1}) was increased by the flow of NO. The $C_xH_yO_z$ amounts decreased by the reaction with NO, although the hydrocarbonate species were more likely to decompose directly to CO_2 and O_2.

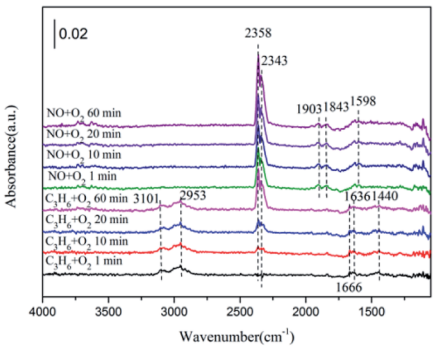

Fig. 9 *In situ* DRIFTS of 5% CeO_2–ZnO exposed to the SCR reaction at 250 °C for various times under C_3H_6 + O_2 adsorption and during NO + O_2 interaction with the C_3H_6 + O_2 gas mixture.

3.6.3. Co-adsorption of C_3H_6 + O_2 with different O_2 content. It is reported that oxygenated hydrocarbon formation is crucial to the production of the $C_xH_yO_z$ species, which are considered to be important intermediates for HC-SCR.[31] In order to understand the reactivity of the partially oxidized species from C_3H_6 due to different O_2 content, the *in situ* DRIFTS spectra of 5% CeO_2–ZnO exposed to C_3H_6 + O_2 with different O_2 content after 30 min are recorded. A similar changing trend was observed in Fig. 10. Spectral features from the hydrocarbon fragment (1442, 2881, 2953 and 3101 cm^{-1}), surface $C_xH_yO_z$ (1636 cm^{-1}) and gas-phase C_3H_6 (1666 cm^{-1}) emerged. With increasing the O_2 content, the intensities of all the peaks significantly increased. This fact indicates that the adsorption and activation of C_3H_6 could be promoted as the O_2 content increased. It is worth noting that the promotion effect was enhanced very slowly as the O_2 content reached 10 vol%. This result implies that the excess O_2 cannot accelerate the C_3H_6 activation and adsorption any more.

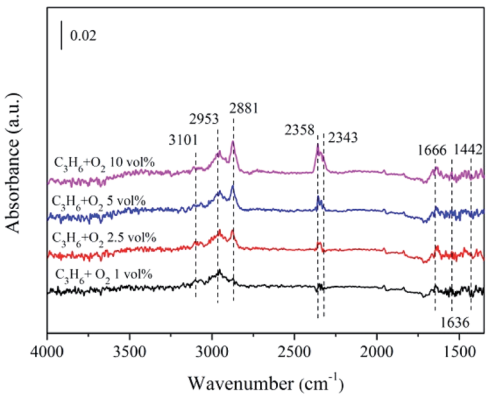

Fig. 10 *In situ* DRIFTS of 5% CeO_2–ZnO exposed to C_3H_6 + O_2 with different O_2 content after 30 min.

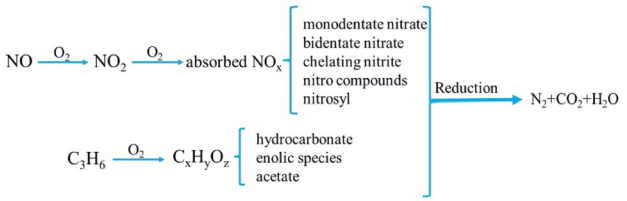

Fig. 11 Proposed reaction mechanism of NO_x reduction by propene over CeO_2–ZnO catalysts.

3.7. Reaction pathway

Many literature reports have confirmed that NO reduction undergoes different reaction pathways, depending on the type of hydrocarbon reductants and SCR catalysts, along with the reaction temperature.[32] In general, two schemes are proposed for the process. One is known as the "decomposition" mechanism, involving the dissociation and adsorption of NO on the metal active sites, followed by the recombination of the adsorbed N to generate the gas-phase N_2. The other is the "reduction" mechanism, which consists of complex surface interactions between the adsorbed NO_x and surface hydrocarbon fragments.[33,34]

In this study, the reaction mechanism of the HC-SCR over the MOF-5-derived CeO_2–ZnO catalysts conforms to the "reduction" mechanism scheme. It can be understood through an analysis of the adsorbed species by means of *in situ* DRIFTS. The scheme of reaction mechanism is shown in Fig. 11. First, during the adsorption and subsequent oxidation of NO process, the nitrates (monodentate nitrates, bidentate nitrates), chelating nitrite, nitro compounds and nitrosyl are generated on the active sites (Ce^{4+} and Zn^{2+}). In addition, an abundance of $C_xH_yO_z$ (enolic species and acetate) is formed and activated on the active sites (Ce^{4+} or Zn^{2+}). Subsequently, in the typical C_3H_6-SCR, the two kinds of surface species above are able to react with each other through the formation of a hydrocarbonate or carbonate species, and then directly produce N_2, CO_2 and H_2O. Based on our present study, these results demonstrate that the Ce addition has a significant positive effect on the formation of more adsorbed NO_x species due to the increase in the available active sites, and contributes to the improvement in the C_3H_6-SCR activity.

4. Conclusions

In summary, the MOF-based derivative x% CeO_2–ZnO ($x = 1$, 3, 5, 10) catalysts were facilely synthesized using a complete thermal decomposition of the Ce/MOF-5 precursor. Combined with XRD, FTIR, TG-DSC, SEM and H_2-TPR experiments, it was found that the as-prepared CeO_2–ZnO catalysts were favorable for strengthening the interaction between Ce^{4+} and Zn^{2+} and exhibited excellent catalytic performance for the C_3H_6-SCR of NO. A significant improvement in the catalytic activity was found over the Ce-doped catalysts with the highest N_2 yield of 69.1% achieved over 5% CeO_2–ZnO. *In situ* DRIFTS and NO-TPD experiments demonstrated the formation of monodentate nitrates, bidentate nitrates, chelating nitrite, nitro compounds, nitrosyl and $C_xH_yO_z$ species (enolic species and acetate) on the surface, and the additional formation of hydrocarbonate or carbonate as intermediates to directly generate N_2, CO_2 and H_2O. Thus, this research highlights new perspectives on the application of MOF materials in the field of deNO_x.

Conflicts of interest

There are no conflicts to declare.

Acknowledgements

This study is supported by the National Natural Science Foundation of China (No. 21866022, 21567018, 51868054), Inner Mongolia Natural Science Foundation (No. 2017MS0214, 2017MS0522), Science and Technology Major Project on Lakes of Inner Mongolia (No. ZDZX2018054), and Inner Mongolia Engineering Research Center of Coal Chemical Wastewater Treatment & Resourcelization.

References

1 G. Pekridis, N. Kaklidis, V. Komvokis, C. Athanasiou, M. Konsolakis, I. V. Yentekakis and G. E. Marnellos, *J. Phys. Chem. A*, 2010, **114**, 3969–3980.
2 P. Granger and V. I. Parvulescu, *Chem. Rev.*, 2011, **111**, 3155–3207.
3 N. A. S. Amin, E. F. Tan and Z. A. Manan, *J. Catal.*, 2004, **222**, 100–106.
4 X. Y. Liu, Z. Jiang, M. X. Chen, J. W. Shi, Z. X. Zhang and W. F. Shangguan, *Ind. Eng. Chem. Res.*, 2011, **50**, 7866–7873.
5 H. A. Habib, R. Basner, R. Brandenburg, U. Armbruster and A. Martin, *ACS Catal.*, 2014, 2479–2491.
6 H. Pan, Y. H. Guo, Y. F. Jian and C. He, *Energy Fuels*, 2015, **29**, 5282–5289.
7 G. Y. Xu, Y. B. Yu and H. He, *ACS Catal.*, 2018, **8**, 2699–2708.
8 Y. H. Hu and K. Griffiths, *Appl. Surf. Sci.*, 2008, **254**, 5048–5054.
9 K. Köhler and C. H. He, *J. Phys. Chem. C*, 2011, **115**, 1248–1254.
10 H. X. Jiang, Q. Y. Wang, H. Q. Wang, Y. F. Chen and M. H. Zhang, *ACS Appl. Mater. Interfaces*, 2016, **8**, 26817–26826.
11 L. Zhang and Y. H. Hu, *Mater. Sci. Eng., B*, 2011, **176**, 573–578.
12 W. Y. Huang, X. Zhou, Q. B. Xia, J. H. Peng, H. H. Wang and Z. Li, *Ind. Eng. Chem. Res.*, 2014, **53**, 11176–11184.
13 Z. J. Li, Y. L. Xiao, W. J. Xue, Q. Y. Yang and C. L. Zhong, *J. Phys. Chem. C*, 2015, **119**, 3674–3683.
14 Q. Naddaf, M. Mansour, H. Thakkar and F. Rezaei, *Ind. Eng. Chem. Res.*, 2018, **57**, 17470–17479.
15 L. Zhang, L. Huang, Y. H. Qin and B. Z. Chen, *Trans. Nonferrous Met. Soc. China*, 2018, **28**, 980–988.
16 X. Chen, X. Chen, E. Q. Yu, S. C. Cai, H. P. Jia, J. Chen and P. Liang, *Chem. Eng. J.*, 2018, **344**, 469–479.

17 K. Cendrowski, P. Skumial, P. Spera and E. Mijowska, *Mater. Des.*, 2016, **110**, 740–748.
18 S. H. Wu, H. J. He, X. Lia, C. P. Yang, G. M. Zeng, B. Wu, S. Y. He and L. Lu, *Chem. Eng. J.*, 2018, **341**, 126–136.
19 L. Qiu, Y. Cheng, C. P. Yang, G. M. Zeng, Z. Y. Long, S. N. Wei, K. Zhao and L. Luo, *RSC Adv.*, 2016, **6**, 17036–17045.
20 Q. L. Zhang, J. Fan, P. Ning, Z. X. Song, X. Liu, L. Y. Wang, J. Wang, H. M. Wang and K. X. Long, *Appl. Surf. Sci.*, 2018, **435**, 1037–1045.
21 Q. Ye, L. N. Yan, H. P. Wang, S. Y. Cheng, D. Wang, T. Kang and H. Dai, *Appl. Catal., A*, 2012, **431–432**, 42–48.
22 A. V. Rajgure, N. L. Tarwal, J. Y. Patil, L. P. Chikhale, R. C. Pawar, C. S. Lee, I. S. Mulla and S. S. Suryavanshi, *Ceram. Int.*, 2014, **40**, 5837–5842.
23 M. Z. Hussain, G. S. Pawar, Z. Huang, A. A. Tahir, R. A. Fischer, Y. Q. Zhu and Y. D. Xia, *Carbon*, 2019, **146**, 348–363.
24 R. Atchudan, T. N. J. I. Edison, S. Perumal, D. Karthikeyan and Y. R. Lee, *J. Photochem. Photobiol., B*, 2016, **162**, 500–510.
25 J. Liu, X. Y. Li, Q. D. Zhao, C. Hao and D. K. Zhang, *Environ. Sci. Technol.*, 2013, **47**, 4528–4535.
26 K. Ueda, J. Y. Ohyama and A. Satsuma, *ACS Omega*, 2017, **2**, 3135–3143.
27 W. Yang, R. D. Zhang, B. H. Chen, D. Duprez and S. Royer, *Environ. Sci. Technol.*, 2012, **46**, 11280–11288.
28 J. Liu, X. Y. Li, Q. D. Zhao, C. Hao, S. B. Wang and M. Tade, *ACS Catal.*, 2014, **4**, 2426–2436.
29 X. X. Cheng, Y. R. Cheng, Z. Q. Wang and C. Y. Ma, *Fuel*, 2018, **214**, 230–241.
30 C. M. Kalamaras, G. G. Olympiou, V. I. Pârvulescu, B. Cojocaru and A. M. Efstathiou, *Appl. Catal., B*, 2017, **206**, 308–318.
31 L. Q. Nguyen, C. Salim and H. Hinode, *Appl. Catal., B*, 2010, **96**, 299–306.
32 J. L. Long, Z. Z. Zhang, Z. X. Ding, R. S. Ruan, Z. H. Li and X. X. Wang, *J. Phys. Chem. C*, 2010, **114**, 15713–15727.
33 M. Haneda, N. Bion, M. Daturi, J. Saussey, J. C. Lavalley, D. Duprez and H. Hamada, *J. Catal.*, 2002, **206**, 114–124.
34 R. Burch, J. P. Breen and F. C. Meunier, *Appl. Catal., B*, 2002, **39**, 283–303.